

# RSC Advances



This is an *Accepted Manuscript*, which has been through the Royal Society of Chemistry peer review process and has been accepted for publication.

*Accepted Manuscripts* are published online shortly after acceptance, before technical editing, formatting and proof reading. Using this free service, authors can make their results available to the community, in citable form, before we publish the edited article. This *Accepted Manuscript* will be replaced by the edited, formatted and paginated article as soon as this is available.

You can find more information about *Accepted Manuscripts* in the [Information for Authors](#).

Please note that technical editing may introduce minor changes to the text and/or graphics, which may alter content. The journal's standard [Terms & Conditions](#) and the [Ethical guidelines](#) still apply. In no event shall the Royal Society of Chemistry be held responsible for any errors or omissions in this *Accepted Manuscript* or any consequences arising from the use of any information it contains.

## ARTICLE

# Facile and controllable synthesis of carbon-encapsulating carbonate apatite nanowires from biomass containing calcium compounds such as $\text{CaC}_2\text{O}_4$ and $\text{CaCO}_3$

Cite this: DOI: 10.1039/x0xx00000x

Received 00th January 2012,  
Accepted 00th January 2012

DOI: 10.1039/x0xx00000x

[www.rsc.org/](http://www.rsc.org/)Namjo Jeong,<sup>\*ab</sup> Seong Ok Han,<sup>a</sup> Heeyeon Kim,<sup>a</sup> Kyo-sik Hwang,<sup>b</sup> SeungCheol Yang,<sup>b</sup> Kahee Kim<sup>c</sup> and Sung-kook Hong<sup>a</sup>

We report the synthesis of carbon-encapsulating carbonate apatite nanowires through a vapor-solid growth by heat-treatment of biomass comprising calcium compounds such as  $\text{CaC}_2\text{O}_4$  or  $\text{CaCO}_3$  at  $900^\circ\text{C}$  using both  $\text{PH}_3$  and  $\text{C}_2\text{H}_2$  as the reactants. The thermal decomposition of  $\text{CaC}_2\text{O}_4$  or  $\text{CaCO}_3$  to  $\text{CaO}$  with increasing temperature ( $\text{CaC}_2\text{O}_4 \rightarrow \text{CaCO}_3 + \text{CO} \rightarrow \text{CaO} + \text{CO}_2$ ) is the key to achieving the growth of such core-shell nanowires. First, vapor-phase reactions between the gaseous calcium species generated from the derived  $\text{CaO}$  and gaseous molecules derived from thermal reactions of the reactants ( $\text{PH}_3$  and  $\text{C}_2\text{H}_2$ ) lead to the oriented growth of core-shell nanowires along the  $[001]$  plane. Second, the  $\text{CO}_2$  generated during the decomposition of  $\text{CaCO}_3$  may be primarily responsible for the incorporation of carbonate ions into apatite structure. Nanowire growth with knots along growth direction reveals that our approach is very controllable. Additional demonstrations using kenaf fibers further verify that other types of biomass too are usable.

## 1. Introduction

Apatite is a very important bio-ceramic for biomedical applications such as biomedical implants, bone regeneration, hard tissue engineering, and drug delivery because it is a major constituent of bones and teeth.<sup>1</sup> Recently, nano-designed apatite structures have drawn keen attention because of their unique properties, which differ from those of their bulk counterparts.<sup>2</sup> One-dimensional (1D) apatite nanostructures such as nanorods, nanotubes, and nanowires are the focus of such studies because their high aspect ratio and unique morphology may help improve bioactivity and mechanical properties of apatite.<sup>3-5</sup> Of particular interest is the interplay that exists between bone cells and nanoscale features, suggesting that these morphologies can provide a favorable environment that enables effective bone cell differentiation and growth.<sup>6,7</sup> In addition to the geometric design, it is also important to functionalize the apatite nanostructures with reinforcing materials such as carbon nanofibers, carbon nanotubes, and graphene because they provide biocompatibility and nanotopographical incentives.<sup>8,9</sup>

We have shown in a recent publication that vertically aligned and carbon-encapsulating apatite nanowires are very attractive structures providing excellent bony fusion and nanoscale reinforcement.<sup>10</sup> Synthesis of the core-shell nanowires was successfully achieved from glass substrate containing  $\text{CaO}$ . In this paper, we show that our concept can be extended to substrates including other calcium compounds such as  $\text{CaC}_2\text{O}_4$  and  $\text{CaCO}_3$ . Also, we discuss in detail the effect of these calcium compounds on the growth mechanism of such

carbon-encapsulating apatite nanowires. For this, we used woody biomass containing  $\text{CaC}_2\text{O}_4$  and egg-shell including  $\text{CaCO}_3$  as starting materials.

Biomass, which is one of the most economical, eco-friendly, and sustainable sources,<sup>11</sup> includes various constituent elements such as Ca, Mg, Na, K, P, and S.<sup>12</sup> Of particular importance are the calcium compounds such as  $\text{CaC}_2\text{O}_4$  and  $\text{CaCO}_3$  it contains.<sup>13</sup> Some studies have provided a tantalizing glimpse of the fabrication of new apatite nanostructures using biomass.<sup>14,15</sup> Furthermore, biomass could be used for fabrication of 1D carbonaceous nanomaterials such as carbon nano-anemones, carbon nanohorn-carbon nanotube hybrids, and cone-shaped graphitic whiskers.<sup>16-18</sup> Therefore, the search for unique carbon-apatite hybrid nanostructures from such promising renewable sources is a very fascinating and significant challenge that can provide new opportunities for fundamental research and technological development in materials science and nanobiotechnology.

Our work focus on the structural changes on transformation of  $\text{CaC}_2\text{O}_4$  or  $\text{CaCO}_3$  into  $\text{CaO}$  during carbonization of biomass to understand the primary responsibility for the generation of the gaseous calcium species that are essential for the vapor-solid (VS) growth of the apatite nanowires. Also, we investigate the effect of  $\text{CO}_2$  derived during the decomposition process of the calcium compounds on the formation of carbonate apatite structure. Some experiments on the effect of synthesis conditions on nanowire growth showed that nanowire growth on the surface of substrates was precipitated when such calcium compounds were decomposed into  $\text{CaO}$ . Interestingly,

as-synthesized apatite crystals grew along the [001] plane, and the controlled nanowire growth with knots along the nanowire growth was possible, which reveals that the chemical reactions responsible for nanowire growth were very controllable. Additionally, we extended this concept to a similar synthesis using different type of woody biomass, thereby verifying that this technique can be used as a general strategy for the fabrication of such hybrid nanostructures that could be used in potential applications.<sup>19,20</sup> Here, we denote the apatite-carbon core-shell nanowires as apatite@carbon nanowires.

## 2. Experimental

### 2.1 Materials

Woody biomasses containing  $\text{CaC}_2\text{O}_4$ , such as henequén fibers (*Agave fourcroydes*) with an average diameter of 150  $\mu\text{m}$  and kenaf fibers (*Hibiscus cannabinus*) with an average diameter of 80–1000  $\mu\text{m}$ , were prepared as starting materials. Henequén fibers were supplied by DESFITSA (Desfibradora Yucateca, S.A.) of Mérida Yucatán, México. The average density was about 1.45  $\text{g}/\text{cm}^3$ . Kenaf fibers were supplied from Bangladesh and have the average density of 1.13  $\text{g}/\text{cm}^3$ . Before heat treatment, the fibers were washed with distilled water for 30 min at room temperature and then dried at 100 °C for 1 day. For thermogravimetric analysis (TGA),  $\text{CaC}_2\text{O}_4 \cdot x\text{H}_2\text{O}$  was purchased from Aldrich. The used chicken egg-shell sample was washed several times with deionized water to remove additional residues and impurities from its surface, and then dried at 110 °C for 1 day.

### 2.2 Synthesis of apatite@carbon nanowires

For synthesis of the apatite@carbon nanowires, the starting materials containing henequén fibers, kenaf fibers, and egg-shell were put in a quartz boat, which was then placed in the center of a quartz reactor. The reactor was rapidly heated at a rate of 45°C/min to the desired temperature, which was controlled between 550 and 900°C, and then held at the raised temperature for 1 h. During the heat treatment, Ar was supplied as the carrier gas at a flow rate of 1000 cc/min. For growth of apatite@carbon nanowires, the concentration of  $\text{PH}_3$  (99.999%) was maintained at 0.01% in Ar, and the concentration of  $\text{C}_2\text{H}_2$  (99.9%) was controlled between 1 and 5% in Ar. After the growth process, the reactor was cooled to room temperature in Ar only.

### 2.3 Characterization

The morphology of the apatite core-carbon heterostructures was observed using scanning electron microscopy (SEM: HITACHI S-4700, operated at 10–15 keV) and transmission electron microscopy (TEM: Tecnai F30 Super-twin, operated at 200 keV). To confirm the composition of the core-shell nanowires, energy dispersive X-ray spectroscopy (EDX: Genesis EDAX) analysis was carried out along with scanning TEM (STEM) using a 1-nm beam diameter. Raman spectroscopy was performed using a JY LabRam HR Raman microscope fitted with a liquid-nitrogen-cooled CCD detector. The Raman spectra were recorded using a backscattering geometry and were obtained under ambient conditions using the 514.5-nm line of an Ar-ion laser. The power level was controlled at 5 mW using a focus spot that was 1  $\mu\text{m}$  in size and lasted for 30 s. The X-ray photoelectron spectroscopy (XPS) was performed using an AXIS-NOVA system (Kratos Inc.) with an X-ray source that emitted monochromatic Al-K $\alpha$  radiation. The area analyzed was 1 mm  $\times$  2 mm, and the base pressure was  $7.0 \times 10^{-7}$  Pa.

The TGA was performed in air using a SDT 2960 Simultaneous DTA-TGA system. The temperature was raised to 1000°C at a rate of 15°C/min, and the Ar carrier gas was supplied at a flow rate of 50 ml/min. The weight of the test samples used for the TGA was approximately 10 mg. Infrared (IR) spectroscopy was recorded using the attenuated total reflection method over the range of 600–4000  $\text{cm}^{-1}$  (HYPERION3000).

Gas chromatograph-mass spectroscopy (GC-MS) analysis was conducted using a 6890 series GC system from Agilent Technologies and a 5973 Network Mass-Selective Detector from Agilent Technologies. The operating parameters were as follows: (a) The columns were 30 m  $\times$  320  $\mu\text{m}$   $\times$  0.25  $\mu\text{m}$  19091J-423 columns for a nitrogen phosphorus detector (NPD, Agilent); (b) The initial temperature of the oven was set to 40°C, which was maintained for 4 min, and the temperature was increased to a final temperature of 200–300°C at the rate of 20°C/min, which was maintained for 6 min; (c) Rubidium beads were used for the NPD; (d) The detector temperature was set to 325°C; (e) The gas conditions for the NPD were Ar at 5 mL/min, air at 60 mL/min, and  $\text{H}_2$  at 3 mL/min; (f) The injection volume was 600  $\mu\text{L}$ , and auto injection was performed at a temperature of 250°C; (g) The run time was 18 min. The detection range for the mass spectrometer was 0–300 M/z, and its scan speed was set at 5.62  $\text{s}^{-1}$ . A gas mixture of 0.01%  $\text{PH}_3$  and 1%  $\text{C}_2\text{H}_2$  in Ar was supplied for the GC-MS analysis.

## 3. Results and discussion

### 3.1. Structural characterization

The henequén fibers used had smooth surfaces before the heat treatment (Fig. 1(a)). When only Ar was supplied during the heat treatment, a corrugated structure was found along the entire length of the resultant carbon fibers (Fig. 1(b)). The surfaces of the carbon fibers appeared slightly rough, but no remarkable nanostructures were observed. The representative EDX spectrum showed that some additional components such as Ca, Na, Mg, and K were included in the carbon fiber (inset of Fig. 1(b)). When a gas mixture of both  $\text{PH}_3$  and  $\text{C}_2\text{H}_2$  was supplied during the heat treatment, on the other hand, the surfaces of the carbon fibers were completely covered with uniform nanowires (Fig. 1(c)) that grew up to 5  $\mu\text{m}$  in length (inset of Fig. 1(c)).

A TEM image and the selected area diffraction (SAED) pattern revealed that the measured  $\{002\}$ ,  $\{211\}$ ,  $\{130\}$ , and  $\{222\}$  families of reflections agree well with those of the hexagonal apatite structure (Fig. 1(d) and (e)).<sup>21</sup> Remarkably, a high-resolution TEM (HRTEM) image showed that the nanowire was composed of defective graphitic layers with thicknesses below 2 nm and a 20-nm-diameter apatite nanowire oriented along the (002) plane (Fig. S1(a)). Furthermore, from the fast Fourier transform (FFT) image, the lattice spacings of the core were calculated to be 3.4, 3.1, and 2.3 Å, which can be assigned to the (002), (210), and (212) planes of hexagonal apatite, respectively (inset of Fig. 2(c)). The EDX spectrum clearly showed the expected Ca, P, O, and C components (Fig. S1(b)).

No Raman excitation peak was observed from the raw henequén fiber (Fig. S2(a)). The Raman spectra of sample heat-treated in Ar only had two prominent bands: D and G bands at 1350 and 1590  $\text{cm}^{-1}$ , respectively. The characteristics of these bands were similar to those of amorphous carbon.<sup>22</sup> The Raman spectrum of the sample that was heat-treated under a gas mixture of both  $\text{PH}_3$  and  $\text{C}_2\text{H}_2$  revealed a very weak peak at approximately 960  $\text{cm}^{-1}$  ( $\text{PO}_4^{3-}(\nu_1)$ ); this peak is a main peak in

the Raman spectra of a typical apatite structure (Fig. S2(b)).<sup>23</sup> The slight enhancement in the intensity ratio of the D to G bands may reflect the effect of the graphitic layers surrounding apatite nanowire (Fig. S2(c)).

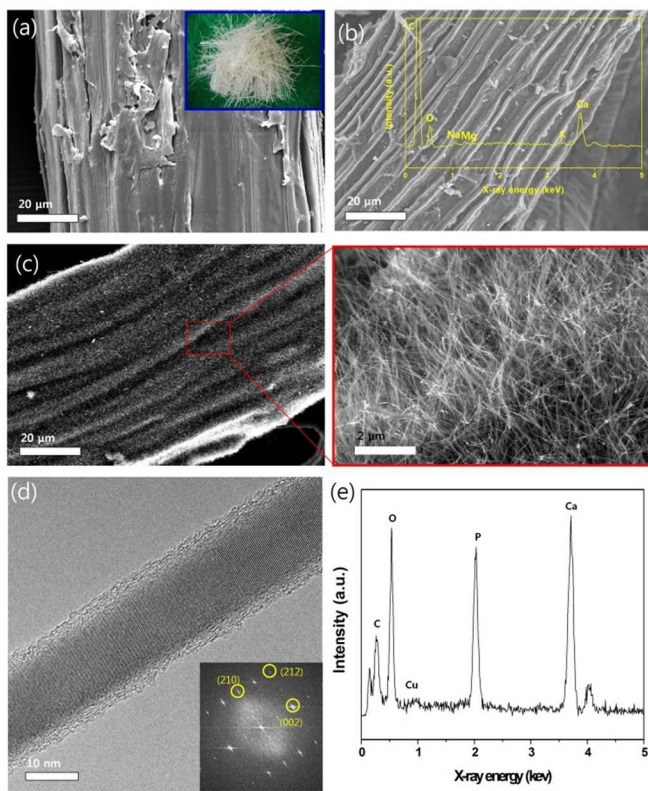


**Fig. 1** (a) SEM image and photograph (inset) of raw henequén fibers. (b) SEM image and EDX spectrum (inset) of carbon fiber obtained after the heat treatment of henequén fibers at 900°C in Ar only. (c) SEM image of nanowire-covered carbon fibers. Inset shows a high-magnification image. (d) HRTEM image showing a nanowire composed of defective graphitic layers and apatite crystal. Inset shows the corresponding FFT image. (e) EDX spectrum of the nanowires. The synthesis was performed for 1 h in a gas mixture of Ar + 0.01% PH<sub>3</sub> + 1% C<sub>2</sub>H<sub>2</sub>.

XPS analysis is of great importance in the determination of the surface composition and chemical state of the products. Fig. 2(a) shows the XPS survey spectra of samples obtained after 1 h of heat treatment at 900°C with an Ar only or Ar + PH<sub>3</sub>/Ar + C<sub>2</sub>H<sub>2</sub> atmosphere. When Ar only was supplied, Ca, O, and C were observed as the main components, but P was absent in the products. The high intensity of the Ca and O peaks reveals that a large number of calcium compounds are present as compared to carbon fiber. On the other hand, when a gas mixture (Ar + PH<sub>3</sub>/Ar + C<sub>2</sub>H<sub>2</sub>) was supplied, peaks corresponding to P were observed in the spectrum. Also, the C peak intensity significantly increased. These changes confirm the formation of carbon-sheathed apatite nanowires on the surface of carbon fibers.

In the detailed XPS spectrum obtained from samples without nanowire growth, the C (1s) peak was deconvoluted into four components (Fig. 2(b)).<sup>24</sup> The main contribution occurred at 284.2 eV, which corresponds to the sp<sup>2</sup>-hybridized graphite-like carbon atom. The sp<sup>3</sup>-hybridized carbon atom,

which is related to disordered carbon and structural defects in graphite sheet, was assigned at 285.6 eV. The carbon atom related to the C-O species was assigned at 286.5 eV. Remarkably, the component assigned to the carboxyl C=O species or carbonate was recorded at a high binding energy of 289.7 eV. These results indicate the presence of CaCO<sub>3</sub> in the samples.<sup>25</sup>

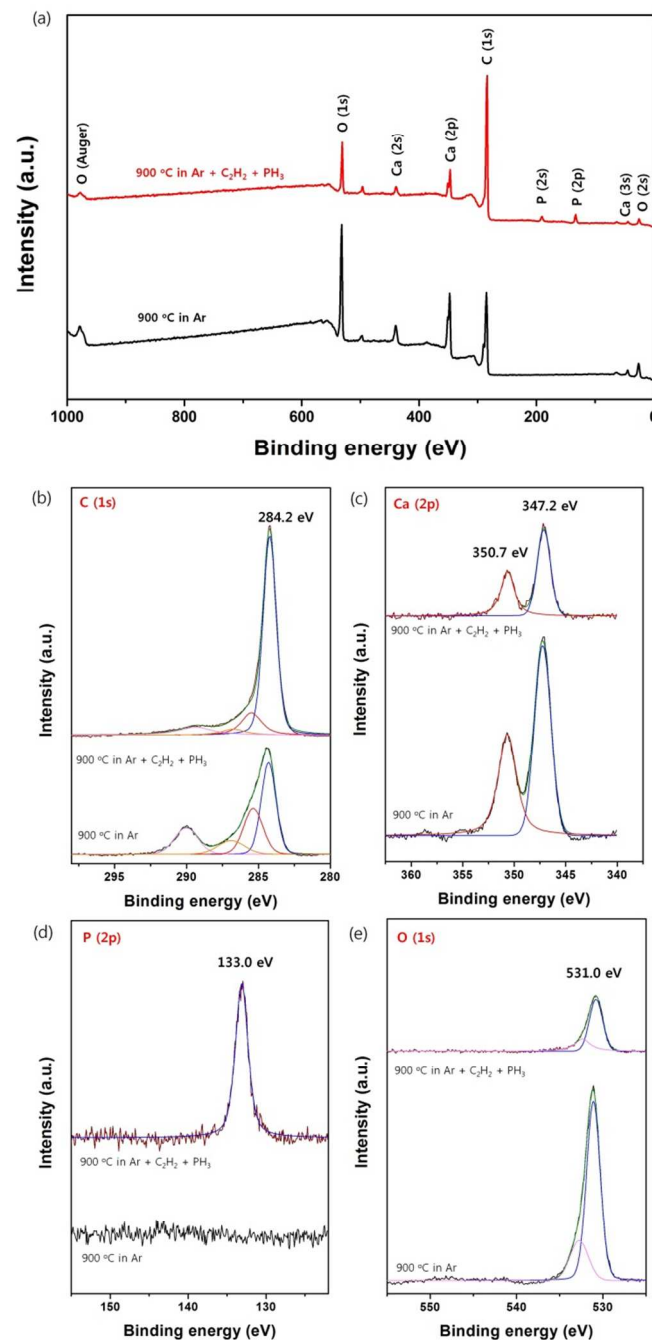


**Fig. 2** (a) The XPS survey spectrum of samples obtained after 1 h of heat treatment at 900°C with an Ar only or Ar + PH<sub>3</sub>/Ar + C<sub>2</sub>H<sub>2</sub> atmosphere, and the detailed scans of (b) C (1s), (c) Ca (2p), (d) P (2p), and (e) O (1s).

The core-level binding energy (BE) positions of Ca ( $2p_{1/2}$ ), Ca ( $2p_{3/2}$ ), and O ( $1s$ ) were at 350.7, 347.2, 133.0, and 531.0 eV, respectively (Fig. 2(c)–(e)). The doublet separation energy of Ca ( $2p$ ) was approximately 3.5 eV. After the nanowire synthesis, the intensity of peak corresponding to C=C increased significantly, which indicates the formation of graphitic layers on the surface of carbon fibers. Furthermore, P ( $2p$ ) was observed at the core-level BE positions of 133.0 eV, which is consistent with that of the phosphate ion.<sup>26</sup> The core-level BE positions of Ca ( $2p_{1/2}$ ), Ca ( $2p_{3/2}$ ), and O ( $1s$ ) was similar to those of the samples without the nanowires. This strongly supports that the apatite structure was formed on the surface of carbon fibers.<sup>27</sup> Furthermore, the weak carbonate peak in C ( $1s$ ) was noticeable, which indicates the following: decomposition of  $\text{CaCO}_3$  to CaO and  $\text{CO}_2$ , and the subsequent incorporation of the carbonate ion into the apatite structure during nanowire synthesis.

The IR spectrum of the sample that was heat-treated under a gas mixture of both  $\text{PH}_3$  and  $\text{C}_2\text{H}_2$  was shown in Fig. S3. The pattern of the absorption peaks is typical for carbonate calcium phosphate.<sup>28,29</sup> The characteristic bands of phosphate groups were observed at about 960 and 1030  $\text{cm}^{-1}$ . The presence of carbonate ions was identified at about 873, 880, 1413, 1458, and 1550  $\text{cm}^{-1}$ , which revealed that carbonate ions were substituted into apatite crystals. Additionally, the peaks measured at about 1370 and 1586  $\text{cm}^{-1}$  indicates the D- and G-bands of graphitic layers encapsulating apatite nanowires.

### 3.2. Growth mechanism

As shown in Fig. 3, the possible mechanism for the formation of carbonate apatite@carbon nanowires can be briefly summarized as follows: nucleation of carbonate apatite crystals, VS growth of carbonate apatite nanowires, and surface graphitization on the radial surfaces of the apatite nanowires.

First, apatite crystals are nucleated on the surface of the carbonized biomass. TGA performed in Ar revealed that the  $\text{CaC}_2\text{O}_4$  crystals decompose between 400 and 525 °C according to the chemical formula  $\text{CaC}_2\text{O}_4 (\text{s}) \rightarrow \text{CaCO}_3 (\text{s}) + \text{CO} (\text{g})$ . Between 660 and 880 °C,  $\text{CaCO}_3$  decomposes into CaO (s) and  $\text{CO}_2$  (g) (Fig. S4).<sup>30</sup> In Fig. S5, gas analysis clearly revealed that  $\text{P}_4$  can be derived from the thermal pyrolysis of  $\text{PH}_3$  at the set temperature of 900 °C. It is also possible that  $\text{P}_4$  may react with oxygen in the reactor, resulting in the formation of phosphorus oxides such as  $\text{P}_4\text{O}_{10}$  (g).<sup>31</sup> Furthermore, a bioactive substrate containing CaO and  $\text{P}_4\text{O}_{10}$  can provide a favorable environment for the formation of calcium phosphate ( $x\text{CaO} (\text{s}) + y\text{P}_4\text{O}_{10} (\text{g}) = \text{Ca}_x(\text{PO}_4)_y (\text{s})$ ), resulting in a transformation to apatite crystal.<sup>32</sup> This supports our hypothesis for the initial formation of nanoscale apatite crystals.

Second, once the apatite is completely crystallized, growth should occur along a particular crystal plane in the axial direction. Biological additives can play a key role in the initial nucleation and oriented crystallization of apatite.<sup>33</sup> Gas analysis clearly revealed that the supply of both  $\text{PH}_3$  and  $\text{C}_2\text{H}_2$  at 900 °C can generate a variety of gaseous molecules such as aromatic hydrocarbon molecules (g),  $\text{H}_2$  (g), phosphine radicals (g),  $\text{P}_4$  (g), and heterocyclic phosphorus compounds such as  $\text{C}_5\text{H}_5\text{P}$  (g). Therefore, it is feasible that the  $\text{C}_5\text{H}_5\text{P}$  (g) may precipitate the nucleation of apatite and lead to the growth of apatite crystals oriented along the [001] plane. Then, oriented apatite crystals start growing along the axial direction. For nanowire growth, calcium- and phosphorus-containing gaseous species should coexist in the reactor. On the other hand, when the reactor temperature rapidly increases to 900 °C, the henequén fibers are

carbonized into amorphous carbon fibers. During this process, the decomposition of  $\text{CaCO}_3$  (s) into CaO (s) generates  $\text{CO}_2$  (g), and calcium-containing gaseous species can be produced from CaO (s). Previous studies have found that the gaseous species that can be generated from CaO (s) include Ca (g), CaO (g),  $\text{O}_2$  (g), and O (g), which are formed by sublimation and dissociation, and Ca (g),  $\text{H}_2$  (g), CaOH (g), and  $\text{Ca}(\text{OH})_2$  (g), which are formed during heating in  $\text{H}_2$  (g).<sup>34,35</sup> Therefore, we speculate that the specific vapor-phase reactions occurring between these gaseous species, particularly between  $\text{P}_4$  (g),  $\text{Ca}(\text{OH})_2$  (g), O (g), and  $\text{CO}_2$  (g), lead to the VS growth of the apatite nanowire.<sup>36</sup> The TGA and IR results clearly revealed the presence of carbonate component in the apatite nanowires. The formation of carbonate is due to the adsorption of  $\text{CO}_2$  derived during the decomposition of  $\text{CaCO}_3$  into CaO (Fig. 3).

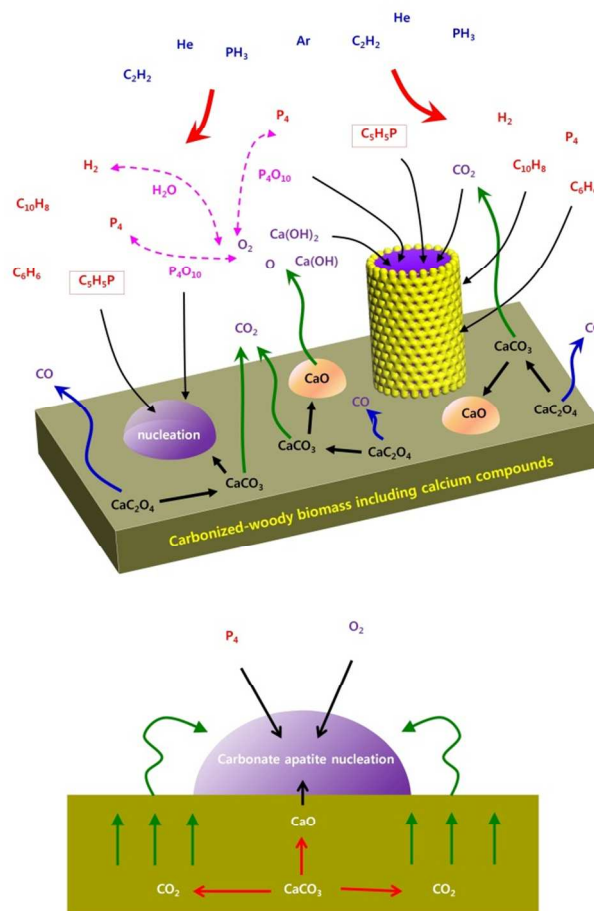


**Fig. 3** Schematic representation of the growth mechanism for a carbonate apatite@carbon nanowire from woody biomass containing  $\text{CaC}_2\text{O}_4$  crystals.

Finally, the surface graphitization should occur simultaneously along the entire radial surface of the apatite nanowires, which have relatively stable interfacial energies. From typical synthetic routes for substrate-based carbon nanotubes, it is acceptable for the interfaces between the nanoscale apatite crystals and the surfaces of the carbon fibers to act as defect sites for the initial formation of graphitic layers.<sup>37</sup> However, the continuous formation of cylindrical graphitic layers is unlikely to be induced through a catalyst-

movement-dependent growth mechanism such as the vapor-liquid-solid growth mechanism. A catalyst-movement-growth mechanism is unlikely not only because the crystalline apatite structures remain in a solid state at the considered temperature but also because they have low carbon solubility and poor catalytic activity. Our gas analysis revealed the presence of aromatic hydrocarbon molecules that are thermally cyclized from  $C_2H_2$  at the set temperature (Fig. S5).<sup>38</sup> Hence, we can hypothesize that these graphitic fragments may be precisely arranged along the radial surface of the carbonate apatite crystals, resulting in continuous formation of the graphitic layers.<sup>39</sup>

### 3.3. Effect of synthesis conditions on nanowire growth

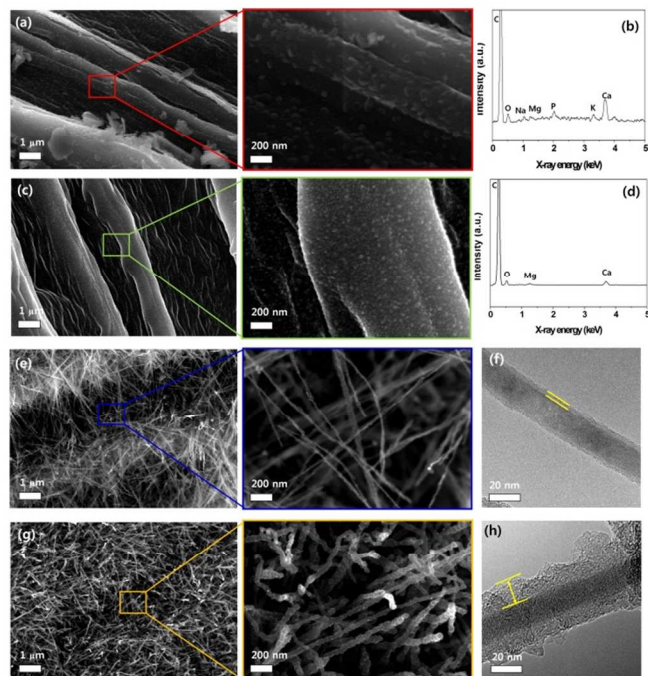


**Fig. 4** SEM images of products heat treated at 900°C with gas mixtures of (a) Ar + 0.01%  $PH_3$ , (c) Ar + 1%  $C_2H_2$ , (e) Ar + 0.01%  $PH_3$  + 1%  $C_2H_2$ , and (g) Ar + 0.01%  $PH_3$  + 5%  $C_2H_2$ . (b) and (d) show the EDX spectrum corresponding to (a) and (c), respectively. (f) and (h) show the TEM images corresponding to (e) and (g), respectively. The insets show the high-magnification images.

We performed two tests to obtain a clearer understanding of the growth mechanism. First, we controlled the synthesis temperature while both  $PH_3$  and  $C_2H_2$  were supplied. At 550°C, nanoparticle formation was observed on the surfaces of the resultant carbon fibers (Fig. S6(a)). The STEM image and its EDX spectrum revealed that the nanoparticles had Ca and P as their primary components (Fig. S6(b) and (c)). The amorphous cores of the nanoparticles were easily vaporized by the short exposure to the electron beam during TEM observations (Fig. S6(d)), resulting in the formation of amorphous hollow carbon nanoparticles (Fig. S6(e)). At the set temperature, the calcium compounds included in the carbon fibers are present as stable  $CaCO_3$  (Fig. S4). The decomposition of  $PH_3$  into phosphorus and hydrogen begins at approximately 375°C and is completed at 593°C,<sup>40</sup> while cyclization of  $C_2H_2$  into aromatic hydrocarbon molecules starts at 650°C (Fig. S5).<sup>38</sup> This implies

the absence of  $C_3H_3P$  (g) molecules that were found to be important for the nucleation and oriented growth of apatite crystals, supporting our results.

Gas analysis showed that a variety of gaseous molecules that were derived at 900°C can also be generated at 750°C (Fig. S5). Therefore, the formation of nanowires composed of crystalline apatite cores and carbon layers may be possible at 750°C (Fig. S7(a)). However, the nanowires generated at 750°C appear short and wavy (Fig. S7(b)). Unlike those synthesized at 900°C, they were easily damaged during TEM observation (arrows in Fig. S7(c)). These differences may be due to the unstable structural change of the included  $CaCO_3$  as the temperature increases (Fig. S4). At 900°C, the complete transformation of  $CaCO_3$  into CaO not only provides a stable site for the nucleation of nanoscale seeds for nanowire growth but also leads to the constant production of calcium-containing gaseous molecules. At 750°C, on the other hand,  $CaCO_3$  does not completely decompose to CaO. This implies that the concentration of the derived calcium-containing gaseous molecules in the reactor is relatively low and continues to change, resulting in the formation of tiny and nonuniform nanowires. This difference may explain why the nanowires were not straight and uniform at 750°C.

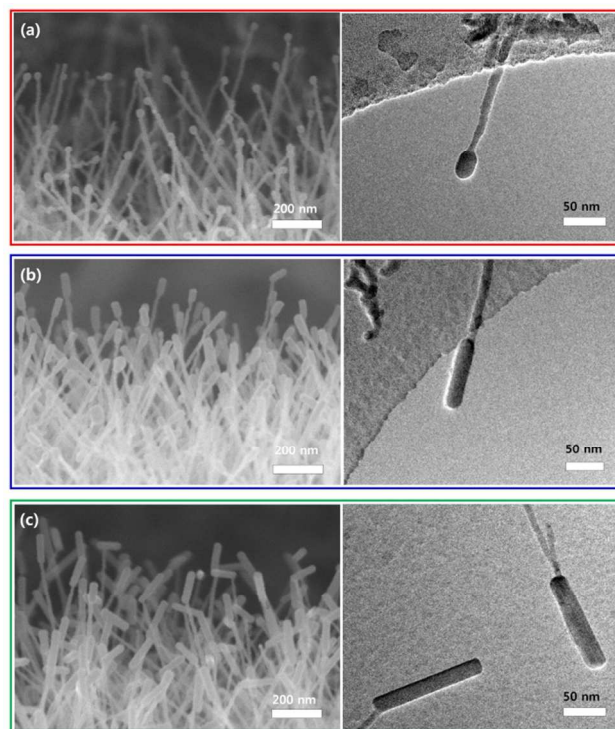


**Fig. 5** SEM and TEM images of nanowires taken at  $C_2H_2$  cut-off times of (a) 3, (b) 5, and (c) 10 min.

Next, we controlled the supply of reactant gases. When only Ar and  $PH_3$  was supplied during the heat treatment, the formation of 100-nm-diameter calcium phosphate nanoparticles was observed on the surface of the carbon fibers (Fig. 4(a) and (b)). After supplying only Ar and  $C_2H_2$ , the nanoparticles with diameter of approximately 20nm were formed on the surface of the carbon fibers (Fig. 4(c)). There are no 1D nanostructures in the resultant products. The EDX spectrum clearly shows that the nanoparticles were inorganic components such as CaO and MgO (Fig. 4(d)). When both  $PH_3$  and  $C_2H_2$  were supplied

together, on the other hand, a dense coverage of uniform nanowires was observed on the carbon fiber surfaces (Fig. 4(e)). The shell thickness of the nanowires was estimated at approximately 2 nm (Fig. 4(f)). These different results strongly indicate that the  $C_5H_5P$  (g) molecules play a key role in the nanowire formation (Fig. S5). Furthermore, when the supplied amount of  $C_2H_2$  was increased, the diameter of the nanowires increased significantly (Fig. 4(g)) because of the increase in the graphitic layer thickness, not because of the apatite cores (Fig. 4(h)). This demonstrates that the surface graphitization is promoted through the enormous accumulation of aromatic hydrocarbon molecules (Fig. S5).

### 3.4. Controlled growth

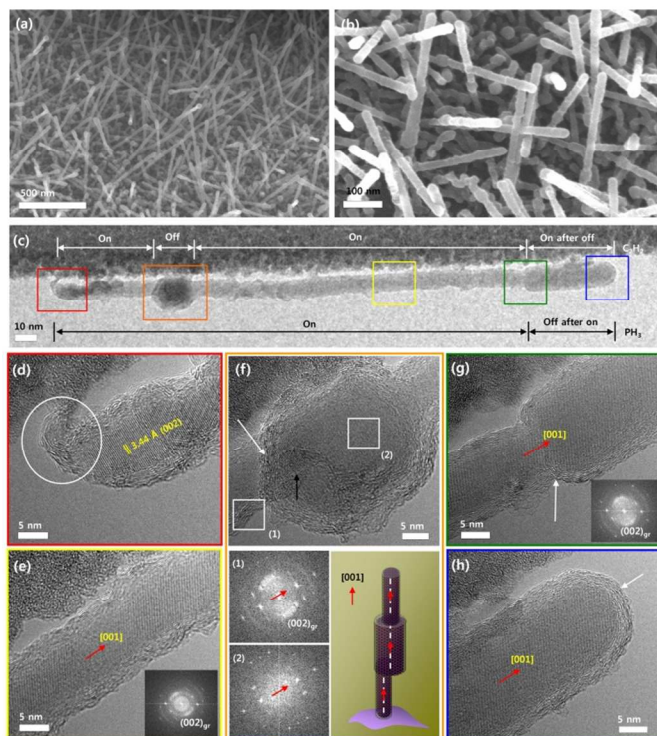


**Fig. 6** Nanowires with two knots formed along the axial growth direction. (a) Low- and (b) high-magnification SEM images. (c) A TEM image of a nanowire obtained by “on” and “off” control of  $PH_3$  and  $C_2H_2$ . HRTEM images taken at the (d) root, (e) stem, (f) first knot, (g) neck, and (h) head of the second knot. The white and black arrows in (f) indicate the graphitic shells observed in the first knot and stem from the mismatch of the growth axes, respectively.

To highlight that our approach is very controllable, we consider the growth of core-shell nanowires with knots along the growth direction. After the 50 min of growth using both  $PH_3$  and  $C_2H_2$ , the  $C_2H_2$  supply was cut off for a short duration. Subsequently,  $C_2H_2$  was re-supplied for 10 min after the  $PH_3$  supply was also cut off. Finally, the reactor was cooled down to room temperature in an Ar atmosphere. As a result, we fabricated nanowires with an enlarged top portion (Fig. 5). The diameter of the nanowires smoothly increased along the neck region. The average diameter of the head was approximately 30 nm and that of the stem was approximately 15 nm. The length of the head was about 50, 100, and 150 nm when the  $C_2H_2$  supply was cut off for 3, 5, and 10 min, respectively (Fig. 5(a)–(c)). Fig. S8(a)

shows the TEM image of nanowires observed at the  $C_2H_2$  cut-off time for 5 min (yellow arrows). The corresponding HRTEM image reveals that the nanowire was completely covered with graphitic layers (Fig. S8(b)), which was confirmed by a virtual image that highlights the graphitic layers in an area selected by a red square in Fig. S8(b) (Fig. S8(c)). In the crystallographic data of both the head and the stem, the lattice spacings of the core had structures that were calculated to be 3.4, 2.8, 3.9, and 4.7 Å, which can be assigned to the (002), (112), (111), and (110) planes of hexagonal apatite (Fig. S8(d) and (e)).

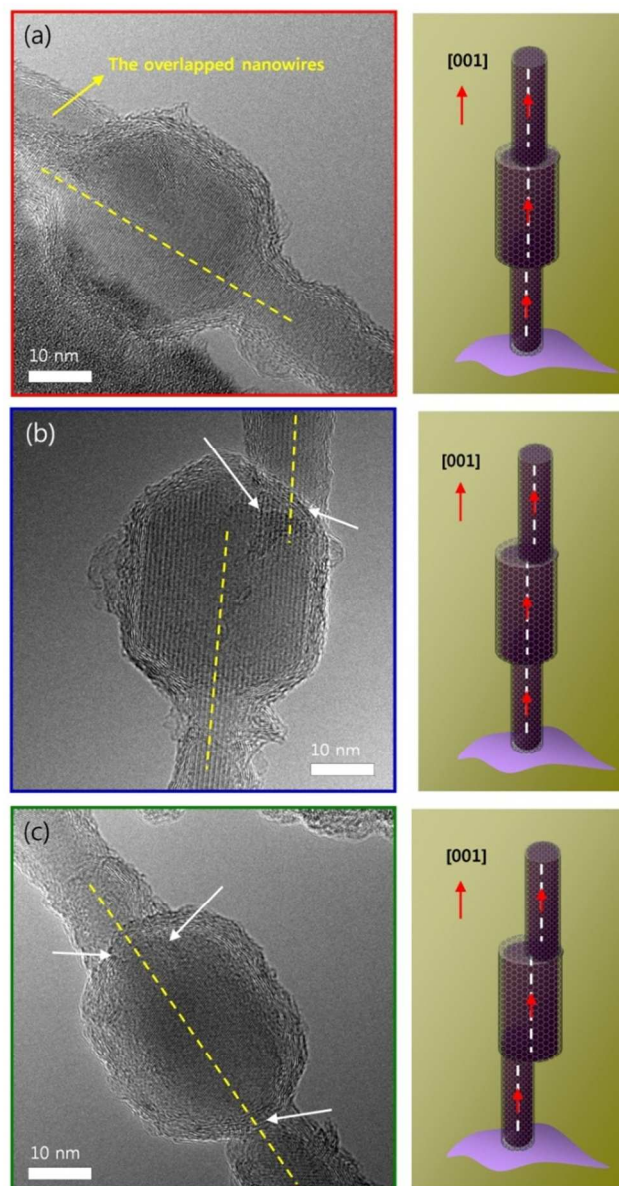


**Fig. 7** (a) The growth axes of two stems completely consistent with that of the knot. (b) The growth axis of the upstream stem is consistent with that of a knot; however, the opposite stem was mismatched. (c) The growth axes of two stems completely dislocated from the knot.

The SEM images show nanowires synthesized with twice the variation of the supplied amount of  $C_2H_2$  (Fig. 6(a) and (b)).

The synthesis time was 60 min. After 20 min of nanowire growth in the presence of both  $C_2H_2$  and  $PH_3$ , the  $C_2H_2$  supply was stopped for 5 min. This process was repeated once more, and then the  $PH_3$  supply was shut off. Finally, only  $C_2H_2$  was re-supplied for 10 min, and the temperature of the reactor was cooled to room temperature. During all processes, Ar was supplied as the carrier gas. Two knots formed along the axial growth direction of the nanowires (Fig. 6(c)). This result was identified from TEM analysis (Fig. 6(d)–(h)). The growth direction and lattice structure did not change throughout the nanowire. The surface of the nanowire was completely covered with graphitic shells except at its root, which seemed to be pulled out (white circle in Fig. 6(d)). It could be inferred from the above results (Fig. 5) that the sheathing of the first knot by graphitic shells was accomplished during the second “on” stage of  $C_2H_2$ . Fig. 6(f) shows the agreement in growth direction as well as the dislocation in the growth axes of the two stems connected to the first knot. The growth of nanowire was orientated along the (001) lattice plane, with an estimated lattice spacing of 3.44 Å.

We speculate that the mismatch in the growth axes of knot and stem of a nanowire is because of the differences between the lateral growth rate of the knot and the formation rate of the graphitic shells on the radial surface of the knot during the growth process (Fig. 7). As mentioned earlier, the formation of graphitic layers suppresses the lateral growth of the apatite core by preventing gaseous sources from being absorbed into the radial surface of the apatite core. Therefore, when only the  $C_2H_2$  supply was stopped, only the lateral growth of the apatite core was allowed (Fig. 5).

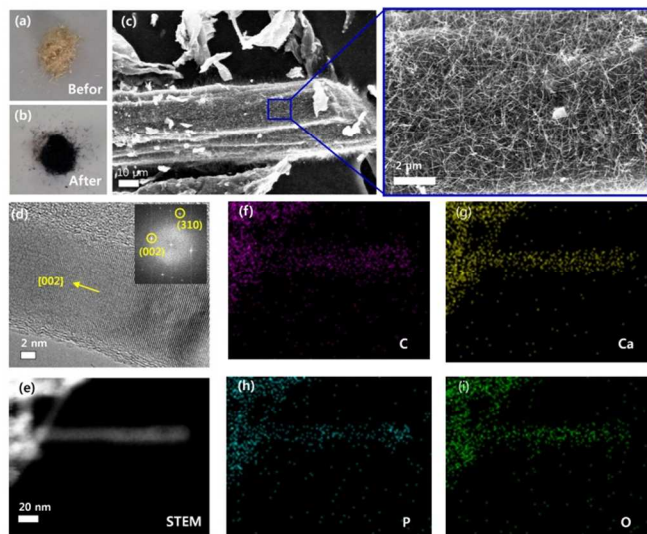


**Fig. 8** Photographs of kenaf fibers (a) before and (b) after synthesis for 1 h at 900°C. SEM images of the products obtained after heat treatments with a gas mixture of (c) Ar + 0.01%  $PH_3$  + 1%  $C_2H_2$ . (d) A TEM image of the as-synthesized nanowire. The inset shows the corresponding FFT image. The lattice spacings of the core were calculated to be 3.4 and 2.2 Å, which can be assigned to the (002) and (310) planes of hexagonal apatite. (e) The scanning TEM image and its corresponding elemental mapping images for (f) C, (g) Ca, (h) P, and (i) O.

If the lateral growth rate stays the same over the entire radial surface of the nanowires, the growth axis of the knots

would coincide with that of stem as shown in Fig. 7(a). On the other hand, Fig. 7(b) shows that the second stem grew with a growth axis dissimilar to that of the first knot. This implies that when  $C_2H_2$  was re-supplied after stopping of knot formation, the formation rate of the graphitic layers depended on the position of the radial surface of the knot. Furthermore, Fig. 7(c) reveals that the growth axes of the two stems are completely dislocated from that of the knot, which indicates an imbalance between the lateral growth rate of the core and the formation rate of the graphitic layers on the core's surface during the change in the reactant supply. Interestingly, it is noteworthy that the growth of all knots and stems of the nanowires was oriented in the [001] direction along the nanowire growth.

### 3.5. Concept expansion

Additional experiment was performed to establish that our approach is very reliable. Kenaf plants are widely known for their contribution to the global and regional environment because of their significant rate of  $CO_2$  accumulation and their high calcium content.<sup>41</sup> Fig. 8 shows the results obtained from kenaf fibers through the same synthesis processes as that performed for the henequén fibers. Nanowires with similar structures were formed on the surface of carbonized kenaf fibers (Fig. 8(a)–(d)). An HRTEM image revealed that the apatite nanowire core oriented along the (002) plane was sheathed in carbon layers (Fig. 8(e) and its inset). The TEM elementary distribution map results confirm the core-shell configuration of the nanowires (Fig. 8(f)–(i)). These results confirm that  $CaC_2O_4$  contained in woody biomass can be very useful in fabricating carbon-functionalized apatite nanostructures.

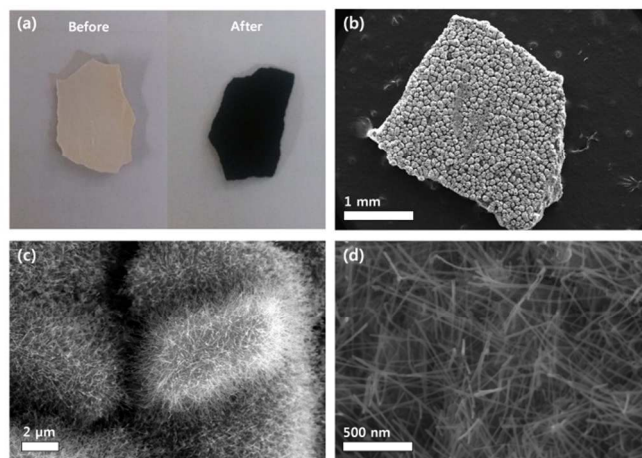


**Fig. 9** Photographs of egg-shell (a) before and after synthesis for 1 h at 900°C. SEM images of the products obtained after heat treatments with a gas mixture of (b-d) Ar + 0.01%  $PH_3$  + 1%  $C_2H_2$ .

The growth mechanism revealed that thermal decomposition of  $CaCO_3$  to  $CaO$  and  $CO_2$  is essential for the growth of carbonate apatite@carbon nanowires. To verify this concept, we employed egg-shell that consists of mostly inorganic calcite (ca. 96%).<sup>42</sup> Recent studies have shown that the major component of the thermal-treated egg-shell was  $CaO$ ,<sup>43</sup> and an egg-shell waste could be used for apatite formation.<sup>42</sup> In this work, we applied the same synthesis

process to egg-shell sample. Fig. 9(a) showed photographs of egg-shell before and after the synthesis process. After synthesizing, the color of egg-shell surface changed to black. Low-magnification SEM image showed a typical mammillae structure of egg-shell (Fig. 9(b)).<sup>44</sup> High-magnification SEM image revealed that whole surface of egg-shell was covered with thin and straight nanowires (Fig. 9(c) and (d)).

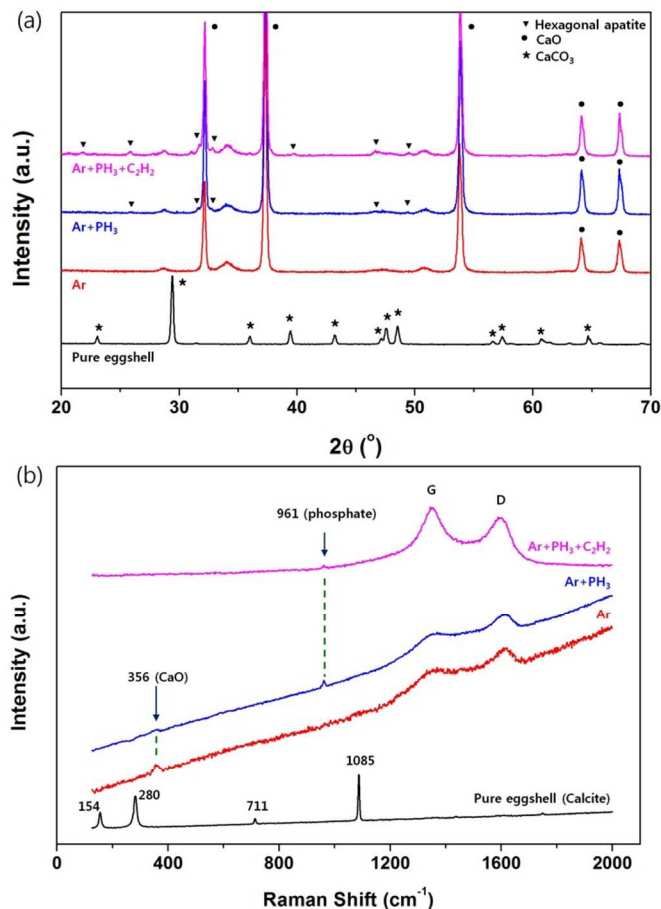


**Fig. 10** (a) XRD and (b) Raman spectra of the samples prepared before and after 1 h of heat treatment at 900°C with an Ar only, Ar + PH<sub>3</sub>/Ar, or Ar + PH<sub>3</sub>/Ar + C<sub>2</sub>H<sub>2</sub> atmosphere.

From XRD graphs (Fig. 10(a)), it was clear that the major component of raw egg-shell was CaCO<sub>3</sub>. After the heat-treatment at 900°C for 1 h in Ar, the CaCO<sub>3</sub> phase was transformed into CaO phase. No peak related to CaCO<sub>3</sub> was observed in the XRD graph. When PH<sub>3</sub> gas was added into the reactor during the heat-treatment, the formation of apatite with hexagonal structure was additionally identified, but the existence of nanowires was not observed on the heat-treated egg-shell surface. When both PH<sub>3</sub> and C<sub>2</sub>H<sub>2</sub> gases was spontaneously supplied into the reactor, on the other hand, the formation of hexagonal apatite structure was remarkable. Fig. 9(d) confirmed that the structure was nanowires with high-yield growth. The Raman spectra supported these results strongly. Furthermore, the characteristics of D- and G- bands of samples obtained after the synthesis process revealed clearly that the nanowires have graphitic structure (Fig. 10(b)).

The EDX spectrum clearly showed the expected Ca, P, O, and C components (Fig. S9). These results indicated that the

suggested growth mechanism can be generally applied to the synthesis processes of unique nanostructures from raw materials that contain calcium compounds such as CaC<sub>2</sub>O<sub>4</sub>, CaCO<sub>3</sub>, and CaO.

## Conclusions

The VS growth of carbonate apatite@carbon nanowires was achieved through the heat treatment of woody biomass at 900°C under a gas mixture of PH<sub>3</sub> and C<sub>2</sub>H<sub>2</sub>. The results clearly showed that structural changes resulting from the conversion of the CaC<sub>2</sub>O<sub>4</sub> or CaCO<sub>3</sub> contained in the biomass to CaO as the temperature increased played an important role in the apatite core growth in the hybrid nanowires. In particular, it is noteworthy that the nucleation and oriented growth of the apatite nanowires was directed by C<sub>5</sub>H<sub>5</sub>P (g) molecules, and that the incorporation of carbonate ions into the apatite structure was attributed to CO<sub>2</sub> generation during the decomposition of CaCO<sub>3</sub> into CaO. The effects of synthesis conditions on the nanowire formation confirmed that the growth mechanism is comparably controllable by changing the temperature or reactants. Similar results were obtained using kenaf fibers and egg-shell. This shows that our approach is very reliable and can be adopted as a general strategy for synthesis of such core-shell nanowires. We anticipate that our concept of using biomass will be developed into an easy method for fabricating new types of nanomaterials in large quantities at low costs and will be a promising avenue for a wide range of potential applications.

## Acknowledgements

This work was conducted under the framework of the Research and Development Program of the Korea Institute of Energy Research (KIER: B4-2452).

## Notes and references

- <sup>a</sup> Energy Materials Research Laboratory, Korea Institute of Energy Research, 71-2, Jang-dong, Yuseong-gu, Daejeon, 305-343, Republic of Korea. E-mail: [nijeong@kier.re.kr](mailto:nijeong@kier.re.kr), [sohan@kier.re.kr](mailto:sohan@kier.re.kr), [sungkookhong@kier.re.kr](mailto:sungkookhong@kier.re.kr); Tel: +82-42-860-3389
- <sup>b</sup> Jeju Global Research Center, Korea Institute of Energy Research, 200, Haemajihaeon-ro, Gujwa-eup, Jeju Special Self-Governing Province, 695-971, Republic of Korea. E-mail: [kshwang@kier.re.kr](mailto:kshwang@kier.re.kr), [pure5258@kier.re.kr](mailto:pure5258@kier.re.kr); Tel: +82-64-800-2229
- <sup>c</sup> Measurement and Analysis Team, Korea Advanced Nanofab Center, 960-10, Iui-dong, Yeongtong-gu, Suwon 443-270, Republic of Korea. E-mail: [nijeong@kier.re.kr](mailto:nijeong@kier.re.kr); Tel: +82-31-546-6319
- † Electronic Supplementary Information (ESI) available. See DOI: 10.1039/b000000x/

- B. Basu, D. S. Katti and A. Kumar, *Advanced biomaterials*, John & Wiley, New Jersey, 2009.
- S. Nayak, B. Satpati, R. K. Shukla, A. Dhawan, S. Bhattacharjee and Y. S. Chaudhary, *J. Mater. Chem.*, 2010, 20, 4949.
- J. Zhan, Y. H. Tseng, J. C. C. Chan and C. Y. Mou, *Adv. Funct. Mater.*, 2005, 13, 2005.
- Y. Xu, J. Jiang, Y. Lu, R. J. Sun, J. Song, L. Rem and S. H. Yu, *Cryst. Growth Des.*, 8, 3822.
- D. O. Costa, S. J. Dixon and A. S. Rizkalla, *ACS Appl. Mater. Interfaces*, 2012, 4, 1490.

- 6 M. M. Stevens and J. H. George, *Science*, 2005, 310, 1135.
- 7 M. J. Dalby, N. Gadegaard, R. Tare, A. Andar, M. O. Riehle, P. Herzyk, C. D. W. Wilkinson and R. O. C. Oreffo, *Nat. Mater.*, 2007, 6, 997-1003.
- 8 D. Lahiri, V. Singh, A. K. Keshri, S. Seal and A. Agarwal, *Carbon*, 2010, 48, 3103.
- 9 M. Wu, Q. Wang, X. Liu and H. Liu, *Carbon*, 2013, 51, 335.
- 10 N. Jeong, M. Cha, Y. C. Park, K. M. Lee, J. H. Lee, B. C. Park and J. Lee, *ACS Nano*, 2013, 7, 5711.
- 11 J. A. Melero, J. Iglesias and A. Garcia, *Energy Environ. Sci.*, 2012, 5, 7393.
- 12 S. Saka and D. A. I. Goring, *Mokuzai Gakkaishi*, 1983, 29, 648.
- 13 M. Jöller, T. Brunner and I. Obernberger, *Energy Fuel*, 2005, 19, 311.
- 14 R. Watanabe, T. Takase and T. Asada, *Carbon*, 2013, 52, 621.
- 15 T. Akaki, H. Maehara and M. Tooyama, *J. Wood Sci.*, 2012, 58, 532.
- 16 M. Zabeti, K. Mojet and K. Seshan, *Carbon*, 2013, 54, 498.
- 17 S. A. M. Zobir, Z. Zainal, C. S. Keng, S. H. Sarijo and M. Yusop, *Carbon*, 2013, 54, 492.
- 18 Y. Saito and T. Arima, *Carbon*, 2007, 45, 248.
- 19 A. A. White, S. M. Best and I. A. Kinloch, *Int. J. Appl. Ceram. Technol.*, 2007, 4, 1.
- 20 M. R. Elahifard, S. Rahimnejad, S. Hahighi and M. R. Gholami, *J. Am. Chem. Soc.*, 2007, 129, 9552.
- 21 J. C. Elliot, *Structure and Chemistry of Apatites and Other Calcium Orthophosphates*, Elsevier, Amsterdam, 1994, pp. 389.
- 22 P. K. Chu, L. Li, *Mater. Chem. Phys.*, 2006, 96, 253.
- 23 M. A. V. M. Grinet, H. Zanin, A. E. C. Granato, M. Porcionatto, F. R. Marciano and A. O. Lobo, *J. Mater. Chem. B*, 2014, 2, 1196.
- 24 V. Datsyuk, M. Kalyva, K. Papagelis, J. Parthenios, D. Tasis, A. Siokou, I. Kallitsis and C. Galiotis, *Carbon*, 2008, 46, 833.
- 25 J. Jiao, X. Liu, W. Gao, C. Wang, H. Feng, X. Zhao and L. Chen, *Crys. Eng. Comm.*, 2009, 11, 1886.
- 26 H. Zeng and W. R. Lacefield, *Biomaterials*, 2000, 21, 23.
- 27 C. C. Chusuei, D. W. Goodman, M. J. Stipdonk, D. R. Justes and E. A. Schweikert, *Anal. Chem.*, 1999, 71, 149153.
- 28 G. Xu, I. A. Aksay and J. T. Groves, *J. Am. Chem. Soc.*, 2001, 123, 2196.
- 29 K. Lin, J. Chang, Y. Zhu, W. Wu, G. Cheng, Y. Zeng and M. Ruan, *Cryst. Growth Des.*, 2009, 9, 177.
- 30 C. Duval, *Inorganic Thermogravimetric Analysis*, Elsevier, New York, 2nd edn, 1963, pp. 281.
- 31 S. Grimme, *J. Chem. Phys.*, 2006, 124, 034108.
- 32 T. Kokubo, H. Kushitani, C. Ohtsuki, S. Sakka and T. Yamamuro, *J. Mater. Sci. Mater. Med.*, 1993, 4, 1.
- 33 J. Tao, H. Pan, Y. Zeng, X. Xu and R. Tang, *J. Phys. Chem. B*, 2007, 111, 13410.
- 34 M. Farber, R. D. Srivastava, J. W. Moyer and J. D. Leeper, *J. Chem. Soc., Faraday Trans.*, 1987, 83, 3229.
- 35 I. O. Samoilova and E. K. Kazenas, *Metalloy*, 1995, 1, 33.
- 36 C. Frondel and E. L. Prien, *Science*, 1942, 95, 431.
- 37 A. Magrez, J. W. Seo, V. L. Kuznetsov and L. Forró, *Angew. Chem. Int. Ed.*, 2007, 46, 441.
- 38 I. Shapiro and H. G. Weiss, *J. Am. Chem. Soc.*, 1957, 79, 3294.
- 39 J. Y. Dai, J. M. Lauerhaas, A. A. Setlur and R. P. H. Chang, *Chem. Phys. Lett.*, 1996, 258, 547.
- 40 A. S. Jordan and A. Robertson, *J. Vac. Sci. Technol. A*, 1994, 12, 204.
- 41 T. B. T. Lam, K. Hori and K. Iiyama, *J. Wood Sci.*, 2003, 49, 255.
- 42 Y. Zhang, Y. Liu, X. Ji, C. E. Banks and W. Zhang, *J. Mater. Chem.*, 2011, 21, 14428.
- 43 T. Witoon, *Ceram. Int.*, 2011, 37, 3291.
- 44 Y. C. Chien, M. T. Hincke, H. Vali and M. D. McKee, *J. Struct. Biol.*, 2008, 163, 84.